Journal of Advanced Ceramics
先进陶瓷
ISSN 2226-4108
CN 10-1154/TQ
清华大学出版社 Tsinghua University Press
SciOpen

J Adv Ceram 2026, **15**: 9221414

https://doi.org/10.26599/JAC.2026.9221414

Research Article

Sintering strategies govern grain and domain evolution for enhanced piezoelectric response in KNN-based lead-free ceramics

Fu Huang[1], Wenfeng Yue[1], Jian Dai[1], Huazhan Gui[1], Konstantin Nefedev[2], Atilla Evcin[3], Gulmurza Abdurakhmanov[4], Nisrin Alnaim[5], Adil Alshoaibi[5,*], Dawei Wang[1,*]

[1] *Precision Acousto-optic Instrument Institute, School of Instrumentation Science and Engineering, Harbin Institute of Technology, Harbin 150080, China*

[2] *Department of Theoretical Physics and Intelligent Technologies, Far Eastern Federal University, Vladivostok 690922, Russian*

[3] *Materials Science and Engineering Department, Afyon Kocatepe University, Afyonkarahisar 03200, Türkiye*

[4] *Faculty of Physics, The National University of Uzbekistan, Tashkent 100174, Uzbekistan*

[5] *Department of Physics, College of Science, King Faisal University, Al-Ahsa 31982, Saudi Arabia*

* Corresponding author.

E-mail: A. Alshoaibi, adshoaibi@kfu.edu.sa;

D. Wang, wangdawei102@gmail.com

Received: October 4, 2026; Revised: November 2, 2026; Accepted: November 18, 2026

©The Author(s) 2026

Just Accepted

Abstract: Lead-free potassium sodium niobate (KNN)-based piezoceramics are highly sensitive to sintering conditions, yet the microstructural origin of this processing dependence remains unclear. Here, a fixed-composition $0.96K_{0.48}Na_{0.52}Nb_{0.96}Sb_{0.04}O_3$–$0.04Bi_{0.5}Na_{0.5}ZrO_3$ (KNNS-BNZ) ceramic was used to isolate the effect of sintering thermal history by comparing conventional sintering (CS), prolonged conventional sintering (PCS), and two-step sintering (TSS). The piezoelectric coefficient (d_{33}) varies markedly with thermal history: CS at 1120 °C for 2 h yields approximately 260 pC/N, extending the dwell to 16 h increases d_{33} to 426 pC/N, and TSS at 1200 °C for 10 min followed by 1100 °C for 7 h further increases d_{33} to 493 pC/N. Across these representative states, the mean grain size increases from 0.77 to 2.11 and 6.57 μm, accompanied by stronger diffraction-peak splitting, larger tetragonal distortion, and a transition from fragmented domains to extended stripe-domain configurations. Polarization measurements further reveal that the coarse-grained TSS specimen retains a larger fraction of the field-induced polarization after field removal, consistent with its more stable remanent state. These results establish a thermal-history-driven processing–structure–property relationship in which grain coarsening and domain reorganization are closely associated with enhanced polarization retention and macroscopic piezoelectric response. This processing–structure–property relationship provides a practical route for optimizing KNN-based ceramics at fixed composition.

Keywords: Potassium sodium niobate; Sintering thermal history; Grain growth; Ferroelectric domains; Piezoelectric response

Just Accepted

1 Introduction

Piezoelectric ceramics enable bidirectional conversion between electrical and mechanical energy and are widely used in transducers, sensors, actuators, and energy-harvesting devices[1–3]. Lead zirconate titanate (PZT)-based ceramics remain dominant in many applications because of their high

electromechanical performance and mature processing technology[4,5]. However, environmental and health concerns associated with lead have driven sustained efforts to develop lead-free alternatives[6,7]. Notably, current RoHS legislation continues to retain specific exemptions for lead in glass or ceramic components used in electrical and electronic equipment[8], underscoring the difficulty of replacing Pb-based functional ceramics across all application spaces. Developing lead-free piezoceramics that combine high performance with robust processing and reliable property reproducibility therefore remains an important objective.

Among lead-free systems, potassium sodium niobate (KNN)-based perovskite ceramics are promising because of their relatively high Curie temperatures and attractive piezoelectric properties[9–11]. Over the past two decades, substantial improvements in KNN-based ceramics have been achieved primarily through compositional engineering, particularly through the construction of polymorphic phase boundaries and regulation of domain structures, with the piezoelectric coefficient (d_{33}) of non-textured ceramics exceeding 650 pC/N[12,13]. However, composition alone does not fully determine the attainable piezoelectric response. KNN ceramics are also highly sensitive to thermal processing, during which densification, volatilization, chemical homogeneity, and grain growth evolve in a strongly coupled manner[14–17]. Despite this sensitivity, sintering has generally been considered mainly from the perspective of densification and process optimization, while the role of the thermal history in establishing the final functional microstructure has received comparatively less attention.

This issue becomes evident from the widely different thermal schedules used to obtain high piezoelectric performance in KNN-based ceramics. Conventional sintering (CS), prolonged conventional sintering (PCS), and two-step sintering (TSS) have all produced high-d_{33} ceramics despite substantial differences in peak temperature and dwell schedule (Fig. 1(a))[12,13,18–20]. More compellingly, large variations in d_{33} persist even when compositional differences are substantially reduced. Compositionally similar Sb-modified KNN (KNNS) systems modified with $Bi_{0.5}Na_{0.5}HfO_3$ (BNH)[21,22] or $Bi_{0.5}(Na_{0.82}K_{0.18})_{0.5}ZrO_3$ (BNKZ)[23,24] exhibit markedly different d_{33} values under

Just Accepted

different thermal histories. Likewise, nominally identical compositions in the $Bi_{0.5}Na_{0.5}ZrO_3$-modified (BNZ) system exhibit pronounced differences in d_{33} under different thermal schedules[25,26]. Similar variations are observed in the BNZ–$BaZrO_3$-modified (BNZ-BZ) system[18,27] (Fig. 1(b)). These comparisons indicate that composition alone cannot account for the large variations in piezoelectric response. They also highlight sintering thermal history as an important factor in establishing the final functional state. Adequate densification is an important prerequisite for favorable piezoelectric properties in KNN-based ceramics[28]. However, the pronounced differences in d_{33} under different thermal histories indicate that densification alone does not fully capture the effects of sintering.

To directly test this inference at fixed composition, $0.96K_{0.48}Na_{0.52}Nb_{0.96}Sb_{0.04}O_3$–$0.04Bi_{0.5}Na_{0.5}ZrO_3$ (KNNS-BNZ) ceramics prepared from the same homogeneous powder batch were subjected to deliberately varied thermal trajectories. Fig. 1(c) compares the green body and three representative sintered states. Conventional sintering at 1120 °C for 2 h yields a d_{33} of approximately 260 pC/N, while the specimen retains an opaque white appearance and shows relatively limited macroscopic shrinkage compared with the green body. In contrast, a brief treatment at 1200 °C for 10 min produces markedly greater macroscopic shrinkage and a more consolidated, translucent appearance (Fig. S1). Despite this pronounced consolidation, the specimen exhibits a very low d_{33} of approximately 24 pC/N. Subsequent holding of this precursor at 1100 °C for 7 h increases d_{33} to 493 pC/N without changing the nominal composition. This direct comparison confirms that pronounced sintering consolidation alone is insufficient to establish a high-piezoelectric-response state.

Accordingly, this work compares conventional, prolonged, and two-step sintering routes to determine how sintering thermal history regulates densification and grain evolution, and how the resulting grain and domain architectures are associated with polarization behavior and piezoelectric response. The research strategy is summarized in Fig. 1(d): adequate densification is considered a prerequisite, while the central focus is to determine how sintering thermal history governs the subsequent grain and domain architecture and thereby controls the piezoelectric response. By

Just Accepted

establishing the relationships among thermal history, grain-scale constraint, lattice and domain architecture, polarization retention, and d_{33}, we aim to clarify how sintering kinetics are translated into functional response. The resulting processing–structure–property framework identifies thermal history as a structural-control parameter at fixed composition and provides a processing route for simultaneously managing densification and the grain and domain architecture required for enhanced piezoelectric response in KNN-based ceramics.

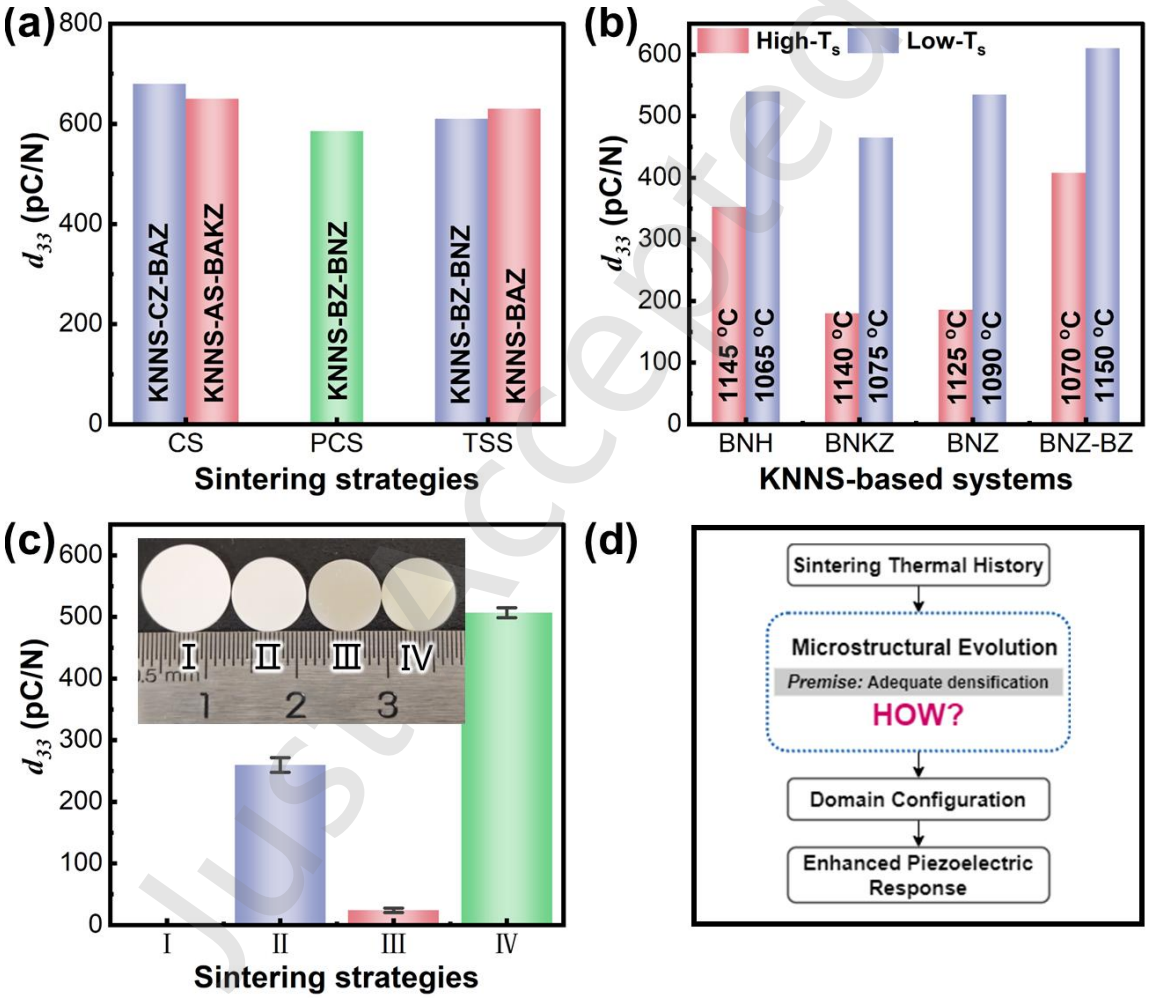


Fig. 1. Effect of sintering thermal history on the macroscopic state and piezoelectric response of KNN-based ceramics. (a) Reported d_{33} values of high-performance KNN-based ceramics prepared by CS[12,13], PCS[20], and TSS[18,19]; (b) d_{33} variation in KNNS-based systems with similar compositions (BNH[21,22] and BNKZ[23,24]) or nominally identical matrices (BNZ[25,26] and BNZ-BZ[18,27]) processed using different thermal schedules; (c) Photographs and corresponding d_{33} values of KNNS-BNZ specimens in four processing states: (I) green body; (II) 1120 °C–2 h (d_{33}≈260 pC/N); (III) 1200 °C–10 min (d_{33}≈24 pC/N); and (IV) 1200 °C–10 min + 1100 °C–7 h (d_{33}≈493 pC/N); (d) Schematic of the processing–structure–property concept examined in this work.

Just Accepted

2 Materials and methods

KNNS-BNZ ceramics with a nominal composition of $0.96K_{0.48}Na_{0.52}Nb_{0.96}Sb_{0.04}O_3$–$0.04Bi_{0.5}Na_{0.5}ZrO_3$ were prepared by a conventional solid-state reaction route. K_2CO_3 (99%, UNID Jiangsu), Na_2CO_3 (99.8%, Xilong Scientific), Nb_2O_5 (99.5%, Jingzhou Mingda Mineral Products), Sb_2O_3 (99.5%, Sinopharm), Bi_2O_3 (99.99%, Sinopharm), and ZrO_2 (99%, Sinopharm) were weighed according to the nominal composition. The hygroscopic carbonates were dried at 180 °C for 12 h before weighing. The powders were mixed with zirconia media in absolute ethanol and planetary ball-milled for 24 h, dried at 80 °C, and calcined at 850 °C for 6 h in a covered alumina crucible. The calcined powder was ball-milled for a further 24 h, dried, granulated with an 8 wt.% poly(vinyl alcohol) aqueous binder, and uniaxially pressed into pellets approximately 10 mm in diameter and 1 mm thick at 40 MPa. Binder burnout was conducted at 650 °C for 2 h using a heating rate of 1 °C/min.

Three sintering routes were investigated in this study, with all heating steps conducted at a rate of 10 °C/min. CS specimens were sintered at 1100–1150 °C for 2 h, with an additional specimen sintered at 1200 °C for 2 h for microstructural comparison. For PCS, the dwell time was extended to 24 h at 1120 °C or 1150 °C. For TSS, specimens were heated to the first-step temperature T_1, held for 10 min, and then cooled at 20 °C/min to $T_2 = T_1 - 100$ °C, followed by a second dwell of 7 h. After completion of the prescribed sintering schedule, all specimens were furnace-cooled to room temperature. For electrical measurements, both parallel surfaces were polished, coated with silver paste, dried at 80 °C, and fired at 600 °C for 30 min. Specimens used for d_{33} measurements were poled in silicone oil at room temperature under a DC field of 30 kV/cm for 20 min and aged for 24 h before testing.

Bulk density was measured by Archimedes' method using deionized water. Room-temperature crystal structures were characterized by X-ray diffraction (XRD; PANalytical EMPYREAN, Netherlands) using Cu Kα radiation, and structural parameters were obtained by Rietveld refinement using Profex[29]. Polarization–electric field (P–E) hysteresis loops were recorded at 1 Hz at room temperature using a ferroelectric analyzer (CPE1901, PolyK, USA). Temperature-dependent relative

Just Accepted

permittivity and dielectric loss of unpoled samples were measured from room temperature to 300 °C at 1 kHz–1 MHz using an impedance analyzer (4980AL, Keysight Technologies, USA) coupled to a high-temperature stage (DMS2000, BALAB, China) at a heating rate of 2 °C/min. The quasi-static piezoelectric charge coefficient d_{33} was measured along the poling direction using a Berlincourt-type meter (ZJ-3A, Institute of Acoustics, Chinese Academy of Sciences).

Surface microstructures and grain morphologies were examined using field-emission scanning electron microscopy (FESEM; TESCAN CLARA, Czech Republic). Mirror-polished samples were thermally etched at 1060 °C for 15 min to reveal grain boundaries for grain-size analysis. Grain size was determined from thermally etched SEM micrographs by directly measuring the linear distance between opposite grain boundaries of individual grains. More than 400 grains were analyzed for each specimen, and the average grain size was calculated as the arithmetic mean of the measured values. Ferroelectric domain patterns were observed on unpoled polished surfaces after chemical etching for 1–2 min in a solution containing equal mass fractions of 37 wt.% HCl and 40 wt.% HF. For piezoresponse force microscopy (PFM, Dimension Icon, Bruker, USA), mirror-polished surfaces were further finished by broad-beam Ar-ion milling (SEM Milling 1061, Fischione, USA) at 3 kV and an incidence angle of 3° for 30 min. Vertical PFM amplitude and phase images were acquired in contact mode using an atomic force microscope equipped with a conductive Co–Cr-coated Si tip, with an AC drive amplitude of 5.0 V and a scan rate of 1.0 Hz. Local switching-spectroscopy PFM measurements were performed using a bipolar triangular DC bias ranging from −10 to +10 V.

High-temperature thermal behavior and sintering shrinkage were further characterized by differential scanning calorimetry-thermogravimetry (DSC–TGA) and dilatometry, respectively; detailed measurement procedures are provided in the Supplementary Information.

3 Results and discussion

3.1 Decoupling densification from piezoelectric response

Just Accepted

For the CS series, bulk density increases overall from approximately 4.06 to 4.30 g/cm^3 as the sintering temperature is raised from 1100 to 1150 °C, whereas d_{33} exhibits a non-monotonic temperature dependence, reaching a maximum of approximately 260 pC/N at 1120 °C before declining at higher temperatures (Fig. 2(a),(d)). Notably, this maximum d_{33} is achieved at a lower density than those of samples sintered at higher temperatures, indicating that increased densification does not necessarily translate into an enhanced piezoelectric response in the present composition.

The PCS series shows a strong dependence on the dwell-temperature window (Fig. 2(b),(e)). At 1120 °C, extending the dwell from 2 to 16 h raises d_{33} from approximately 260 to 426 pC/N before a subsequent decrease at longer times. At 1150 °C, however, prolonged holding produces only a modest maximum d_{33} of approximately 169 pC/N near 8 h. The contrasting dwell-time dependences at 1120 and 1150 °C demonstrate that the effect of prolonged sintering on d_{33} is strongly temperature dependent and cannot be explained by densification alone.

A similar divergence between bulk density and piezoelectric response is observed in the TSS series (Fig. 2(c), (f)). The bulk density increases rapidly to approximately 4.45 g/cm³ when T_1 reaches 1180 °C and subsequently remains relatively high. In contrast, d_{33} exhibits a non-monotonic dependence on the thermal schedule. The maximum d_{33} of 493 pC/N is achieved at 1200 °C–10 min + 1100 °C–7 h, whereas the value decreases to 172 pC/N at 1230 °C–10 min + 1130 °C–7 h. Notably, the 1150 °C-10 min + 1050 °C-7 h specimen, despite its lower bulk density of approximately 4.04 g/cm^3, exhibits a d_{33} of 311 pC/N, exceeding the maximum value obtained in the CS series. These results further demonstrate that maximizing bulk density alone is insufficient to maximize d_{33} and that the piezoelectric response is strongly dependent on the specific thermal trajectory. Accordingly, the 1120 °C-2 h, 1120 °C-16 h, and 1200 °C-10 min + 1100 °C-7 h specimens were selected as representative CS, PCS, and TSS states, respectively, for the subsequent structural analyses.

Just Accepted

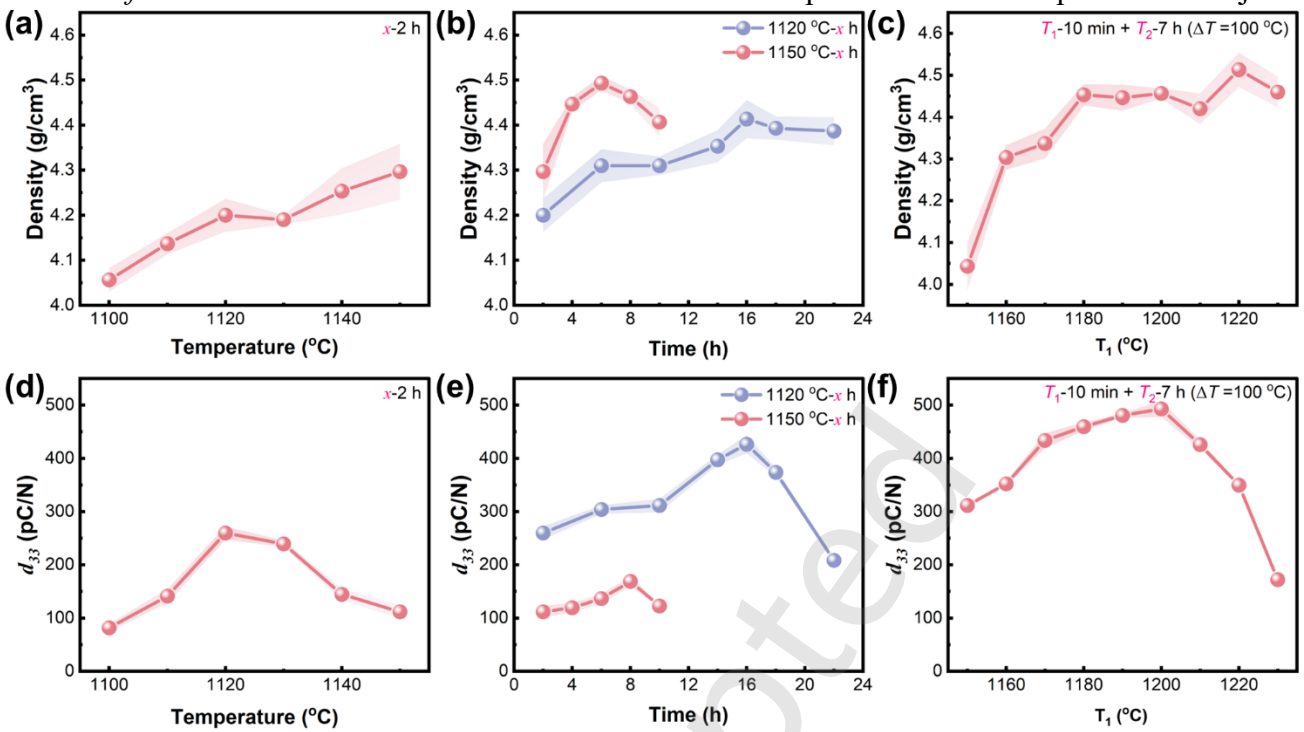


Fig. 2. Bulk density and d_{33} of KNNS-BNZ ceramics under different sintering thermal histories. (a,d) CS series as a function of sintering temperature with a fixed dwell time of 2 h; (b,e) PCS series as a function of dwell time at 1120 and 1150 °C; (c,f) TSS series as a function of T_1, with $T_2 = T_1 - 100$ °C and dwell times of 10 min and 7 h at T_1 and T_2, respectively. The plotted values represent the mean of at least three specimens ($n \geq 3$) for each sintering condition, and the shaded bands indicate ± one standard deviation (SD).

3.2 Crystal structure and microstructure

All samples retain the characteristic diffraction features of the perovskite structure, with no obvious secondary-phase reflections detected (Fig. 3(a–c)). The most pronounced processing-dependent changes occur in the $2\theta \approx 45$–$46°$ region. For the CS series, the reflections remain essentially unresolved at 1100–1110 °C, develop clear peak splitting at 1120–1130 °C, and show diminished splitting again at higher temperatures (Fig. 3(a)). Prolonged holding at 1120 °C further sharpens the separated reflections, whereas the 1150 °C PCS series is characterized mainly by peak broadening without a distinct doublet-like feature (Fig. 3(b)). In comparison, the TSS series exhibits well-defined peak splitting over a relatively broad processing window, although the splitting becomes blurred again under the highest-temperature condition of 1230 °C-10 min + 1130 °C-7 h (Fig. 3(c)).

Rietveld refinements are provided in Fig. S2 and Table S1. The 1100 °C-2 h specimen can be represented by a pseudocubic (PC) average structure, whereas the representative CS, PCS, and TSS

Just Accepted

specimens are described using coexisting rhombohedral (R, R3m), orthorhombic (O, Bmm2), and tetragonal (T, P4mm) components, with the T phase remaining dominant. Importantly, the refined tetragonal fractions of the three representative states remain within a relatively narrow range despite their markedly different d_{33} values. The temperature-dependent dielectric spectra (Fig. S3) likewise show typical ferroelectric transition features. Taken together, these results indicate that average phase fractions alone cannot account for the large processing-induced differences in piezoelectric response.

The tetragonal axial ratios c_T/a_T calculated from Table S1 are approximately 1.0062, 1.0074, and 1.0076 for the CS, PCS, and TSS specimens, respectively (Fig. 3(e)). Although a modest increase in tetragonal distortion is observed from CS to PCS and TSS, the overall variation in c_T/a_T is limited, particularly between the PCS and TSS states. This relatively small structural variation is insufficient to account for the pronounced differences in d_{33}, indicating that additional microstructural factors beyond the average crystal structure must be involved. Grain architecture and domain configuration are therefore considered in the following sections.

Just Accepted

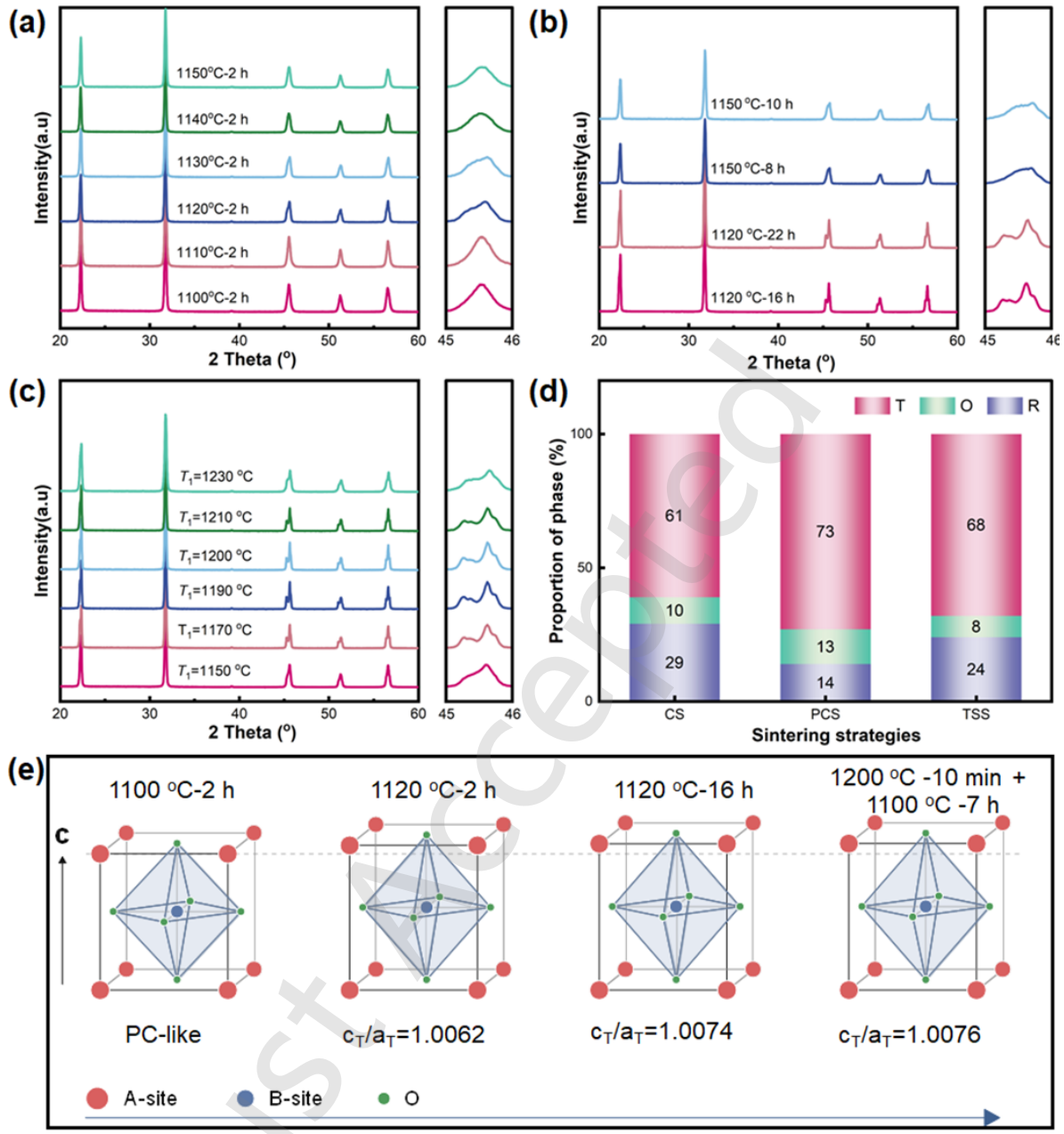


Fig. 3. XRD characteristics and refined crystal structures of KNNS-BNZ ceramics under different sintering thermal histories. (a) XRD patterns of the CS series sintered at 1100–1150 °C for 2 h, with enlarged profiles of the 2θ ≈ 45–46° region; (b) XRD patterns of the PCS series with prolonged dwell times at 1120 and 1150 °C, together with the corresponding enlarged peak profiles; (c) XRD patterns of the TSS series obtained by varying T_1 while maintaining $T_2 = T_1 - 100$ °C, with dwell times of 10 min and 7 h at T_1 and T_2, respectively; (d) Rietveld-refined R, O, and T phase fractions of the representative CS (1120 °C-2 h), PCS (1120 °C-16 h), and TSS (1200 °C-10 min + 1100 °C-7 h) specimens; (e) Schematic comparison of the pseudocubic-like structure of the 1100 °C-2 h specimen and the tetragonally distorted structures of the representative CS, PCS, and TSS specimens, with corresponding c_T/a_T values of 1.0062, 1.0074, and 1.0076, respectively.

Just Accepted

Thermally etched microstructures under representative sintering thermal histories are shown in Fig. 4. The 1120 °C-2 h specimen is relatively porous and fine-grained, with an average grain size of 0.77 μm and a maximum observed grain size of 2.29 μm (Fig. 4(a)). Notably, grain size does not increase monotonically with sintering temperature. The 1150 °C–2 h specimen exhibits a finer grain structure than the 1120 °C–2 h specimen. Further increasing the temperature to 1200 °C still does not induce appreciable grain coarsening (Fig. 4(a–c)). The 1200 °C-2 h specimen remains dense but fine-grained, with average and maximum grain sizes of approximately 0.53 and 1.94 μm, respectively. The effect of prolonged holding is likewise strongly temperature dependent. At 1120 °C, extending the dwell from 2 to 16 h markedly reduces porosity and increases the average grain size to 2.11 μm, with grains up to 10.42 μm (Fig. 4(a),(d)). In contrast, extending the dwell at 1150 °C from 2 to 10 h produces only limited grain growth, with the maximum grain size remaining approximately 2.42 μm (Fig. 4(b),(e)). The TSS specimen processed at 1200 °C-10 min + 1100 °C-7 h exhibits the most pronounced coarsening, with an average grain size of 6.57 μm and a maximum observed size of 30.12 μm (Fig. 4(f)). These comparisons demonstrate that grain growth is not a monotonic function of either sintering temperature or dwell time, but depends strongly on the specific thermal history.

The staged TSS experiments further distinguish the evolution of densification from that of grain growth (Fig. S4). Direct sintering at 1100 °C-2 h leaves a highly porous fine-grained structure with an average grain size of approximately 0.31 μm (Fig. S4(a)). After 1200 °C-10 min, the average grain size increases only to approximately 0.50 μm while porosity is markedly reduced (Fig. S4(f)), indicating that the short high-temperature step primarily establishes a dense fine-grained precursor. After a subsequent dwell at 1100 °C for 2 h, a bimodal microstructure containing grains larger than 20 μm together with numerous submicrometre grains develop (Fig. S4(g)). Here, abnormal grain growth (AGG) is identified by the disproportionate enlargement of a subset of grains relative to the surrounding fine-grained matrix, resulting in a highly heterogeneous or bimodal grain-size distribution. This morphology is consistent with the onset of abnormal grain growth during the second step and

Just Accepted

indicates that the preceding high-temperature treatment substantially alters the subsequent grain-growth trajectory. This staged evolution helps explain why the final TSS specimen develops a markedly coarser grain structure than the PCS specimen despite its substantially shorter total dwell time.

DSC and dilatometry provide complementary information on the temperature range relevant to the TSS process (Fig. S5). The DSC curve shows a pronounced endothermic event beginning at approximately 1170 °C and peaking near 1234 °C, marking a distinct thermal event in this temperature range. More importantly, dilatometry shows continued shrinkage during isothermal holding at 1110 °C after cooling from the high-temperature stage, demonstrating that mass transport and microstructural evolution remain active during the second TSS step. Together with the staged SEM observations (Fig. S4(f),(g)), these results support a processing sequence in which the short high-temperature step establishes a dense fine-grained precursor, whereas the subsequent lower-temperature dwell permits continued microstructural evolution and the onset of abnormal grain growth. This evolution strongly depends on the selected temperature window. The lower-temperature TSS condition of 1150 °C–10 min + 1050 °C–7 h retains fine grains and unclosed pores (Fig. S4(h)). Increasing the TSS temperatures to 1230 °C–10 min + 1130 °C–7 h also suppresses pronounced grain coarsening (Fig. S4(i)). Thus, increasing the sintering temperature does not monotonically promote grain growth, either under conventional/prolonged sintering or under a two-step thermal schedule.

Just Accepted

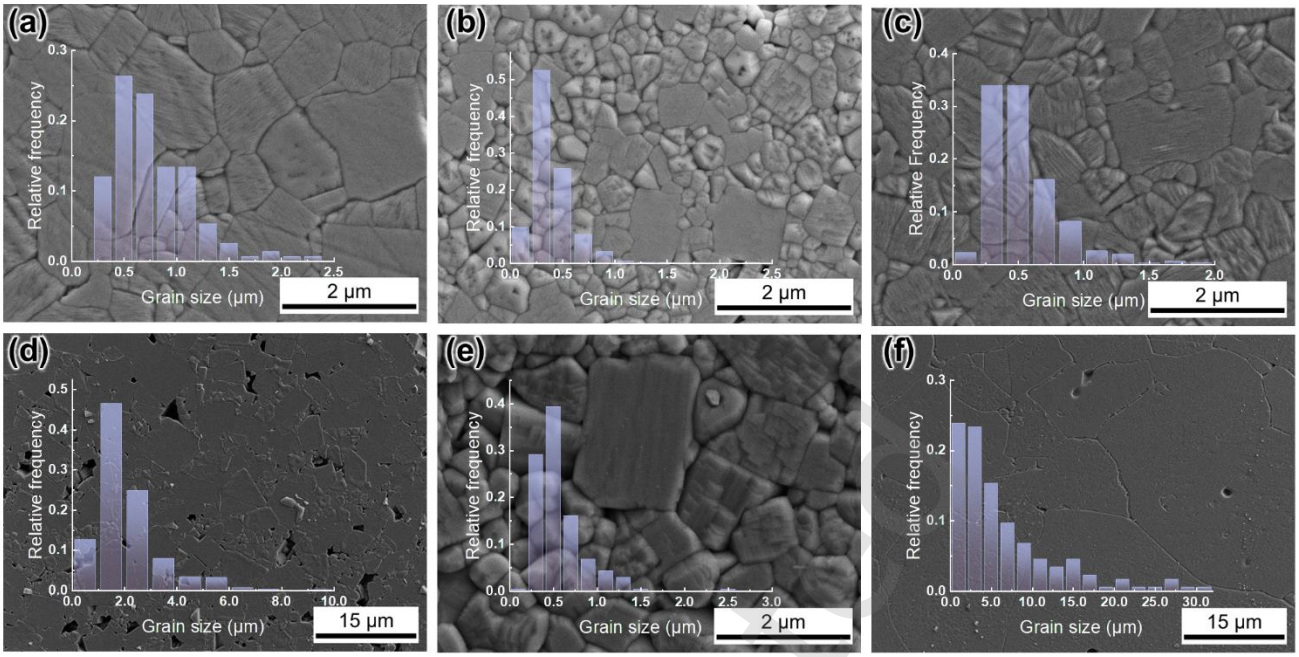


Fig. 4. Thermally etched SEM microstructures and corresponding grain-size distributions of KNNS-BNZ ceramics under representative sintering thermal histories. (a–c) Specimens sintered for 2 h at (a) 1120 °C; (b) 1150 °C; (c) 1200 °C; (d,e) Specimens subjected to prolonged sintering at (d) 1120 °C-16 h; (e) 1150 °C-10 h; (f) Specimen processed by TSS at 1200 °C-10 min + 1100 °C-7 h.

3.3 Domain architecture and polarization behavior

Chemically etched microstructures reveal a systematic evolution of the domain pattern (Fig. 5a–d). The representative CS specimen is dominated by fine, spatially confined domain features, with stripe-like domains observed only locally in larger grains and exhibiting a representative local width of approximately 100 nm (Fig. 5(a)). Continuous stripe domains also remain scarce in the 1150 °C-10 h specimen (Fig. 5(b)). In contrast, the representative PCS specimen exhibits multidirectional stripe-domain clusters within enlarged grains, with representative local widths of approximately 132 and 268 nm (Fig. 5(c)). The representative TSS specimen develops the most extended and continuous stripe-domain architecture, with representative local stripe widths of approximately 226 and 343 nm (Fig. 5(d)). Overall, the domain morphology evolves with grain coarsening from fragmented and spatially confined patterns toward extended, continuous stripe-domain configurations.

The P–E loops show a corresponding difference in polarization retention (Fig. 5(e),(f)). For the fine-grained CS sample, maximum polarization (P_{max}) continues to increase with electric field while

Just Accepted

remanent polarization (P_r) remains substantially lower, giving a large P_{max}–P_r separation (26.4 μC/cm^2 to 19.2 μC/cm^2). This behavior indicates that progressively more polarization can be activated under stronger fields, but a considerable fraction of the field-induced state is not retained after unloading. In the coarse-grained TSS specimen, the loop approaches saturation at a lower field and the P_{max}–P_r separation (27.5 μC/cm^2 to 21.8 μC/cm^2) is smaller, demonstrating a more stable remanent polarization state. These results provide direct macroscopic evidence that the two domain architectures follow different field-induced polarization and post-field relaxation pathways.

PFM measurements provide independent local-scale evidence for this distinction (Fig. 6). The CS specimen exhibits predominantly patchy and fragmented amplitude and phase contrast (Fig. 6(b),(c)), whereas the TSS specimen shows continuous, nearly parallel stripe-like modulation with a representative local width of approximately 154 nm (Fig. 6(e),(f)). The correspondence between chemically etched SEM and PFM therefore supports the development of a continuous stripe-domain architecture in the coarse-grained state rather than an imaging-specific surface artifact.

Both specimens exhibit local phase reversal accompanied by amplitude minima near the switching-bias region, confirming switchable ferroelectric polarization (Fig. 6(h)). The TSS specimen shows a higher piezoresponse amplitude over most of the applied-bias range than the CS specimen, consistent with a stronger local electromechanical response (Fig. 6(g)). Together with the macroscopic P–E and d_{33} results, these PFM measurements further support the close association between thermal-history-induced domain reorganization, polarization retention, and electromechanical response.

Just Accepted

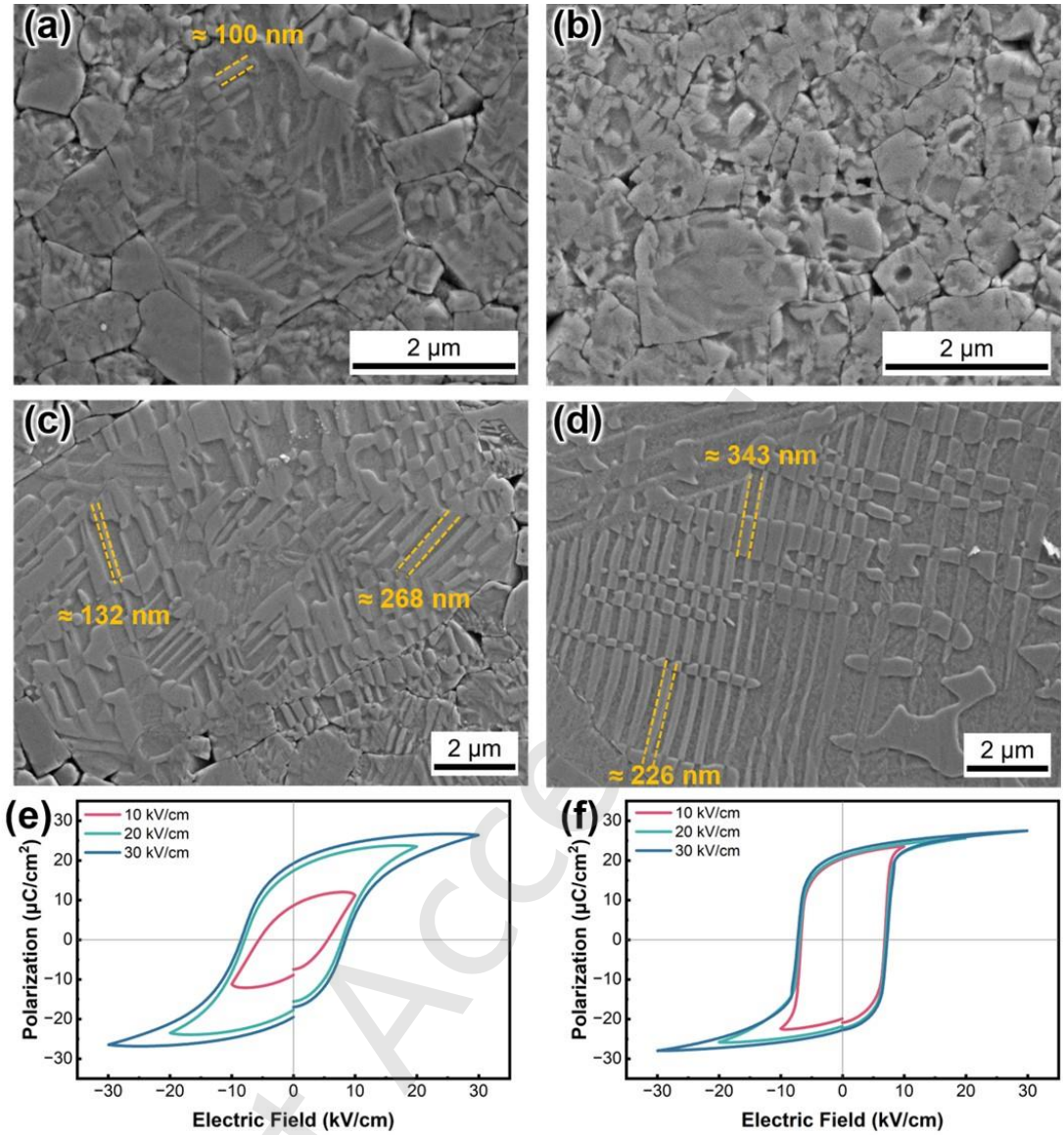


Fig. 5. Chemically etched SEM images of specimens processed at (a) 1120 °C-2 h; (b) 1150 °C-10 h; (c) 1120 °C-16 h; (d) 1200 °C-10 min + 1100 °C-7 h; (e,f) P–E hysteresis loops of the representative: (e) CS specimen (1120 °C-2 h) and (f) TSS specimen (1200 °C-10 min + 1100 °C-7 h) measured under different electric fields.

Just Accepted

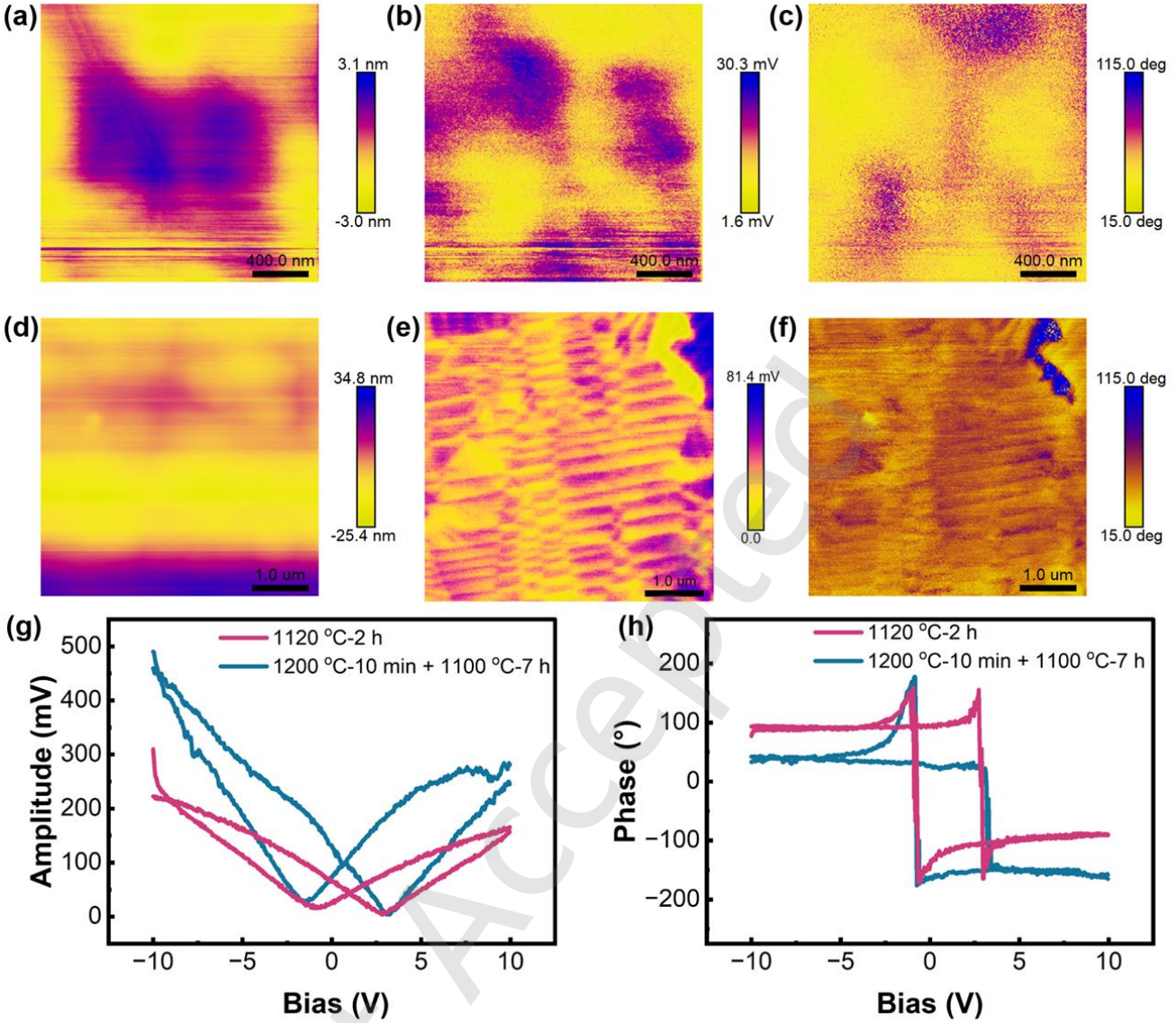


Fig. 6. PFM domain structures and local switching responses of the representative CS and TSS specimens. (a–c) Surface topography, PFM amplitude, and phase images of the CS specimen (1120 °C-2 h); (d–f) Corresponding images of the TSS specimen (1200 °C-10 min + 1100 °C-7 h); (g) Local amplitude–bias loops; (h) Local phase–bias hysteresis loops. PFM amplitude is reported in instrument output units (mV); scan sizes and color-bar ranges are indicated in the individual panels. The CS and TSS specimens were characterized using the same probe type and consistent acquisition settings.

Just Accepted

3.4 Discussion

The combined results indicate that densification and grain growth do not evolve synchronously during sintering and exhibit distinct temperature dependences. At relatively low temperatures, insufficient thermal activation limits mass transport and grain-boundary migration, resulting in porous fine-grained microstructures. Increasing the sintering temperature markedly promotes pore elimination and densification, whereas grain coarsening does not increase monotonically, allowing dense but still

fine-grained states to form at higher temperatures. The TSS route follows a distinct staged pathway: the short high-temperature step first establishes a dense fine-grained precursor, while the subsequent lower-temperature dwell promotes pronounced grain coarsening and the onset of abnormal grain growth. The continued shrinkage during isothermal holding at 1110 °C further supports that mass transport and microstructural evolution remain active during the second step. Thus, the final grain architecture is governed not simply by the peak sintering temperature or dwell time, but by the specific thermal trajectory through which densification and grain growth proceed. Such non-monotonic grain-growth behavior is consistent with previously reported non-Arrhenius grain evolution in KNN-based ceramics[30–32].

Alkali volatilization is another potential factor affecting the properties of KNN-based ceramics during sintering. In the present TSS process, the high-temperature dwell at 1200 °C was limited to 10 min. The TGA curve exhibits an overall mass increase upon heating to approximately 1200 °C, while the XRD patterns show no detectable secondary phases. Moreover, the representative CS, PCS, and TSS specimens exhibit low room-temperature dielectric losses, without a pronounced increase after TSS treatment. Although minor alkali loss cannot be entirely excluded, these observations do not indicate severe volatilization-related degradation. More importantly, d_{33} increases from approximately 24 pC/N after the short high-temperature treatment to 493 pC/N following the subsequent 1100 °C–7 h dwell, accompanied by pronounced grain coarsening. These results highlight the critical role of microstructural evolution during the second sintering stage in achieving the enhanced piezoelectric response.

The resulting grain architecture provides a physical basis for the markedly different domain configurations observed in the representative specimens. Grain boundaries impose mechanical compatibility constraints on ferroelastic deformation and can restrict non-180° domain switching and wall motion[33,34]. This effect is particularly important in fine-grained ceramics because ferroelastic domain formation and reorientation are accompanied by spontaneous strain that must be

Just Accepted

accommodated by neighboring grains. Accordingly, the high grain-boundary density of the CS state favors spatially confined and fragmented domain configurations. Grain coarsening progressively relaxes these mechanical constraints, allowing ferroelastic variants to reorganize and self-accommodate over larger length scales. Classical ferroelastic-twinning analyses show that multidomain configurations can reduce elastic energy through strain accommodation[35,36]. Consistent with this principle, the observed domain morphology evolves from fragmented configurations in the CS specimen to multidirectional stripe-domain clusters in the PCS specimen. The TSS specimen further develops an extended and continuous stripe-domain architecture. Although the local stress state was not directly quantified, the systematic correspondence between grain size and domain morphology supports this constraint-mediated interpretation. This interpretation also helps explain why the 1200 °C–10 min precursor exhibits a very low d_{33} of approximately 24 pC/N despite its translucent appearance: the reduced porosity favors light transmission, whereas its fine-grained microstructure remains subject to strong grain-boundary constraints that limit the piezoelectric response.

These distinct domain architectures are further manifested in the field-dependent polarization response. In the fine-grained CS specimen, increasing electric field progressively increases P_{max}, indicating that additional polarization states can still be activated under stronger fields. However, a substantial fraction of the induced polarization is lost after field removal, resulting in a large P_{max}–P_r separation. This behavior is consistent with limited cooperative ferroelastic switching and pronounced back-switching or relaxation toward the mechanically constrained initial state[34]. In contrast, the extended stripe-domain network in the coarse-grained TSS specimen provides greater freedom for cooperative variant redistribution and domain-wall motion. Consequently, polarization approaches saturation more readily, and a larger fraction of the field-induced polarization is retained after unloading, giving rise to a higher P_r and a smaller P_{max}-P_r difference. The domain architecture therefore governs not only the field-driven polarization pathway but also the stability of the remanent state.

Just Accepted

Although the increased tetragonal distortion may contribute to the enhanced piezoelectric response, its relatively small variation, particularly between the PCS and TSS specimens, cannot fully account for the observed differences in d_{33}. Instead, the evolution of grain and domain architecture provides a more direct physical basis for the enhanced small-signal piezoelectric response. Reversible domain-wall motion is a well-established extrinsic contribution to the piezoelectric response of ferroelectric ceramics[37,38]. The continuous stripe-domain configurations observed in the TSS specimen, together with its higher local PFM response, are therefore consistent with a larger reversible domain-wall contribution than in the fragmented fine-grained CS state.

4 Conclusions

By varying the sintering thermal history of a fixed KNNS-BNZ composition, we demonstrate that sufficient densification is a prerequisite for favorable piezoelectric response, but that maximum densification does not necessarily yield the highest d_{33}. The representative CS, PCS, and TSS states exhibit d_{33} values of approximately 260, 426, and 493 pC/N, respectively, while their mean grain sizes increase from 0.77 to 2.11 and 6.57 μm. The enhancement in d_{33} is accompanied by more pronounced diffraction-peak splitting, increased tetragonal distortion, and a clear evolution from fragmented local domains to extended stripe-domain configurations. In contrast, the refined macroscopic phase fractions vary within a relatively narrow range and do not track the large variation in d_{33}, indicating that average phase constitution alone is insufficient to determine the piezoelectric response.

Together, these results establish a processing–structure–property relationship governed by sintering thermal history. Different sintering strategies regulate densification, grain architecture, and lattice distortion. These structural changes, in turn, modify the mechanical boundary conditions for ferroelastic domain formation and reorganization. In the optimized TSS route, the short high-temperature step establishes a dense fine-grained precursor, whereas the subsequent lower-temperature dwell promotes pronounced grain coarsening and abnormal grain growth. The resulting coarse-grained state, characterized by reduced grain-boundary constraint and an extended stripe-domain architecture,

Just Accepted

retains a larger fraction of the field-induced polarization and exhibits a stronger local electromechanical response. The enhanced d_{33} therefore arises from the coupled evolution of grain architecture, lattice structure, domain configuration, and polarization retention, rather than from density or average phase constitution alone. More broadly, the results identify sintering thermal history as an active processing variable for engineering the microstructural and ferroelectric states that determine the piezoelectric response of KNN-based ceramics.

Acknowledgements

The authors extend their gratitude to Shiyanjia Lab (www.shiyanjia.com) for the DSC and DIL measurements.

Funding

This work was financially supported by the National Natural Science Foundation of China (No. 52472122) and Deanship of Scientific Research, Vice Presidency for Graduate Studies and Scientific Research, King Faisal University, Saudi Arabia (Grant No. KFU253744).

Author contributions

Fu Huang: Writing – original draft, Investigation. Wenfeng Yue: Data curation. Jian Dai: Formal analysis. Huazhan Gui: Methodology. Konstantin Nefedev: Writing – review & editing. Atilla Evcin: Writing – review & editing. Gulmurza Abdurakhmanov: Writing – review & editing. Nisrin Alnaim: Writing – review & editing. Adil Alshoaibi: Writing – review & editing, Funding acquisition. Dawei Wang: Writing – review & editing, Supervision, Funding acquisition.

Availability of data and materials

The data that support the findings of this study are available from the corresponding author upon reasonable request.

Competing interests

The authors have no competing interests to declare that are relevant to the content of this article.

Just Accepted

Electronic Supplementary Material (ESM)

Supplementary material containing additional experimental details, Rietveld refinement results, dielectric spectra, microstructural characterization, and thermal/dilatometric analyses is available in the online version of this article.

References

[1] Qin H, Zhao J, Chen X, *et al.* Investigation of lead-free $BiFeO_3$–$BaTiO_3$ piezoelectric ceramics through precise composition control. *J Adv Dielectr* 2023, **13**: 2350018.

[2] Dai J, Fan Z, Xie H, *et al.* Versatile $BiFeO_3$ shining in piezocatalysis: from materials engineering to diverse applications. *J Adv Ceram* 2025, **14**: 9221046.

[3] He R, Guo H, Yao Z, *et al.* Negligible-hysteresis piezoceramic achieved by multiphase assisting and domain configuration manipulating. *J Adv Ceram* 2025, **14**: 9221160.

[4] Zhao J, Qin H, Chen X, *et al.* Enhanced piezoelectric properties and electrical resistivity in $CaHfO_3$ modified $BiFeO_3BaTiO_3$ lead-free piezoceramics. *J Materiomics* 2024, **10**: 416–22.

[5] Song Y, Yue W, Cheng M, *et al.* Structural evolution and energy storage performance in SBLT-based thin films by high-entropy engineering. *J Materiomics* 2026: 101321.

[6] Qin H, Zhao J, Chen X, *et al.* Investigation of $BiFeO_3$-$BaTiO_3$ lead-free piezoelectric ceramics with nonstoichiometric bismuth. *Microstructures* 2023, **3**: 2023035.

[7] Dai J, Zhu Y, Fan Z, *et al.* Synergistic mechanical nanostructuring and peroxymonosulfate activation enable superior piezocatalysis. *Microstructures* 2026, **6**: 2026043.

[8] Tabeshfar M, Anandakrishnan SS, Bai Y. Recycled piezoelectric materials with competitive second-life functional properties. *Adv Electron Mater* 2026, **12**: e00726.

[9] Qi X, Ren P, Tong X, *et al.* Enhanced piezoelectric properties of KNN-based ceramics by synergistic modulation of phase constitution, grain size and domain configurations. *J Eur Ceram*

Just Accepted

Soc 2025, **45**: 116874.

[10] Qi X, Ren P, Tong X, *et al.* Simultaneous regulation of piezoelectric performance and its temperature stability via the construction of multiscale heterostructures in KNN-based ceramics. *Chem Eng J* 2025, **524**: 168277.

[11] Qi X, Ren P, Tong X, *et al.* Improved grain size homogeneity, enhanced piezoelectric and mechanical properties of potassium sodium niobate-based ceramics. *J Am Ceram Soc* 2025, **108**: e20483.

[12] Tao H, Wu H, Liu Y, *et al.* Ultrahigh performance in lead-free piezoceramics utilizing a relaxor slush polar state with multiphase coexistence. *J Am Chem Soc* 2019, **141**: 13987–94.

[13] Go SH, Kim DS, Eum JM, *et al.* Excellent piezoelectric properties of (K,Na)(Nb,Sb)O_3-$CaZrO_3$-(Bi,Ag)ZrO_3 lead-free piezoceramics. *J Alloys Compd* 2021, **889**: 161817.

[14] Huang F, Yue W, Dai J, *et al.* Optimizing the d_{33}–T_C trade-off in KNN-based piezoceramics via trace $AgSbO_3$ doping. *Ceram Int* 2026, **52**: 8374–81.

[15] Thong HC, Zhao C, Zhu ZX, *et al.* The impact of chemical heterogeneity in lead-free (K,Na)NbO_3 piezoelectric perovskite: ferroelectric phase coexistence. *Acta Mater* 2019, **166**: 551–9.

[16] Chang Y, Yang Z, Hou Y, *et al.* Effects of Li content on the phase structure and electrical properties of lead-free $(K_{0.46-x2}Na_{0.54-x2}Li_x)(Nb_{0.76}Ta_{0.20}Sb_{0.04})O_3$ ceramics. *Appl Phys Lett* 2007, **90**: 232905.

[17] Zhen Y, Li J. Abnormal Grain Growth and New Core–Shell Structure in (K,Na)NbO_3 -Based Lead-Free Piezoelectric Ceramics. *J Am Ceram Soc* 2007, **90**: 3496–502.

[18] Zhou C, Zhang J, Yao W, *et al.* Remarkably strong piezoelectricity, rhombohedral-orthorhombic-tetragonal phase coexistence and domain structure of (K,Na)(Nb,Sb)O_3–(Bi,Na)ZrO_3–$BaZrO_3$ ceramics. *J Alloys Compd* 2020, **820**: 153411.

[19] Xue H, Huang X, Sun X, *et al.* Superior lead-free piezoceramics for wearable multimodal

Just Accepted

ultrasound imaging arrays. *Nat Commun* 2025, **17**: 218.

[20] Liu Y, Fan J, Qi X, *et al.* Adaptive ferroelectric states in KNN-based piezoceramics: Unveiling the mechanism of enhancing piezoelectric properties through multiple phase boundary engineering. *Nano Energy* 2024, **128**: 109972.

[21] Jia P, Zheng Z, Li Y, *et al.* The achieving enhanced piezoelectric performance of KNN-based ceramics: Decisive role of multi-phase coexistence induced by lattice distortion. *J Alloys Compd* 2023, **930**: 167416.

[22] Zhang J, Sun X, Su W, *et al.* Superior piezoelectricity and rhombohedral-orthorhombic-tetragonal phase coexistence of $(1-x)$(K,Na)(Nb,Sb)O3$-x$(Bi,Na)HfO_3 ceramics. *Scr Mater* 2020, **176**: 108–11.

[23] Zhang Y, Wang S, Chen C, *et al.* Enhanced linearity of KNNS-BNKZ ceramics by combining the controls of phase composition and microstructure. *Ceram Int* 2018, **44**: 8380–6.

[24] Wu J, Wang X, Cheng X, *et al.* New potassium-sodium niobate lead-free piezoceramic: giant-d_{33} vs. sintering temperature. *J Appl Phys* 2014, **115**: 114104.

[25] Zhang J, Zhou C. Study of domain configurations in (Bi,Na)ZrO_3-modified (K,Na)(Nb,Sb)O_3 piezoelectric ceramics by acid-etching at different temperatures. *Sci Rep* 2020, **10**: 18526.

[26] Li Y, Jia P, Zhao R, *et al.* Nanoscale domains in $K_{0.48}Na_{0.52}Nb_{0.96}Sb_{0.04}O_3$ – $Bi_{0.5}Na_{0.5}ZrO_3$ ceramics enhance piezoelectric properties. *Mater Chem Phys* 2022, **277**: 125575.

[27] Ma J, Wu B, Wu W, *et al.* Structure and electrical properties of $(0.99-x)K_{0.5}Na_{0.5}Nb_{0.96}Sb_{0.04}O_3-0.01BaZrO_3$-$xBi_{0.5}Na_{0.5}ZrO_3$ lead-free piezoelectric ceramics. *J Mater Sci Mater Electron* 2018, **29**: 12323–9.

[28] Liu Y, Bin C, Sun C, *et al.* Enhanced piezoelectric performance in KNN-based ferroelectric ceramics through a synergistic strategy design. *Ceram Int* 2026, **52**: 23107–17.

[29] Doebelin N, Kleeberg R. Profex: A graphical user interface for the rietveld refinement program BGMN. *J Appl Crystallogr* 2015, **48**: 1573–80.

Just Accepted

[30] Cheng Y, Wu Y, Mo M, *et al.* Improving non-sensitivity of sintering behavior in KNN-based ceramics via Fe_2O_3 doping. *J Alloys Compd* 2023, **955**: 170288.

[31] Liu Z, Cai W, Zhang Q, *et al.* Dielectric and ferroelectric properties of KNN ceramics fabricated by microwave sintering. *J Electron Mater* 2024, **53**: 7170–8.

[32] Lin J, Peng J, Wang S, *et al.* Enhanced extrinsic piezoelectric contribution and microscopic origin of grain size effect in lead-free KNN-based ceramics. *ACS Appl Mater Interfaces* 2026, **18**: 49441–53.

[33] Schultheiß J, Checchia S, Uršič H, *et al.* Domain wall-grain boundary interactions in polycrystalline $Pb(Zr_{0.7}Ti_{0.3})O_3$ piezoceramics. *J Eur Ceram Soc* 2020, **40**: 3965–73.

[34] Li FX, Rajapakse RKND. A constrained domain-switching model for polycrystalline ferroelectric ceramics. Part I: Model formulation and application to tetragonal materials. *Acta Mater* 2007, **55**: 6472–80.

[35] Arlt G. Twinning in ferroelectric and ferroelastic ceramics: Stress relief. *J Mater Sci* 1990, **25**: 2655–66.

[36] Cao W, Cross LE. Theory of tetragonal twin structures in ferroelectric perovskites with a first-order phase transition. *Phys Rev B* 1991, **44**: 5–12.

[37] Damjanovic D. Contributions to the piezoelectric effect in ferroelectric single crystals and ceramics. *J Am Ceram Soc* 2005, **88**: 2663–76.

[38] Pramanick A, Damjanovic D, Daniels JE, *et al.* Origins of electro-mechanical coupling in polycrystalline ferroelectrics during subcoercive electrical loading. *J Am Ceram Soc* 2011, **94**: 293–309.

Just Accepted